Linking Atmospheric River Hydrological Impacts on the U.S. West Coast to Rossby Wave Breaking

HUANCUI HU, FRANCINA DOMINGUEZ, AND ZHUO WANG

Department of Atmospheric Sciences, University of Illinois at Urbana–Champaign, Urbana, Illinois

DAVID A. LAVERS[a]

Scripps Institution of Oceanography, La Jolla, California

GAN ZHANG

Department of Atmospheric Sciences, University of Illinois at Urbana–Champaign, Urbana, Illinois

F. MARTIN RALPH

Scripps Institution of Oceanography, La Jolla, California

(Manuscript received 16 May 2016, in final form 25 January 2017)

ABSTRACT

Atmospheric rivers (ARs) have significant hydrometeorological impacts on the U.S. West Coast. This study presents the connection between the characteristics of large-scale Rossby wave breaking (RWB) over the eastern North Pacific and the regional-scale hydrological impacts associated with landfalling ARs on the U.S. West Coast (36°–49°N). ARs associated with RWB account for two-thirds of the landfalling AR events and >70% of total AR-precipitation in the winter season. The two regimes of RWB—anticyclonic wave breaking (AWB) and cyclonic wave breaking (CWB)—are associated with different directions of the vertically integrated water vapor transport (IVT). AWB-ARs impinge in a more westerly direction on the coast whereas CWB-ARs impinge in a more southwesterly direction.

Most of the landfalling ARs along the northwestern coast of the United States (states of Washington and Oregon) are AWB-ARs. Because of their westerly impinging angles when compared to CWB-ARs, AWB-ARs arrive more orthogonally to the western Cascades and more efficiently transform water vapor into precipitation through orographic lift than CWB-ARs. Consequently, AWB-ARs are associated with the most extreme streamflows in the region.

Along the southwest coast of the United States (California), the southwesterly impinging angles of CWB-ARs are more orthogonal to the local topography. Furthermore, the southwest coast CWB-ARs have more intense IVT. Consequently, CWB-ARs are associated with the most intense precipitation. As a result, most of the extreme streamflows in southwest coastal basins are associated with CWB-ARs. In summary, depending on the associated RWB type, ARs impinge on the local topography at a different angle and have a different spatial signature of precipitation and streamflow.

1. Introduction

Precipitation related to atmospheric rivers (Zhu and Newell 1998; Ralph et al. 2004) is critically important for water resources on the West Coast of the United States. Between 25% and 50% of the annual precipitation falling on the West Coast is related to atmospheric river (AR) events (Dettinger et al. 2011), and ARs are responsible for a large fraction of the snow water equivalent accumulated in the Sierra Nevada mountains (Guan et al. 2010). ARs, by definition, are filamentary structures characterized by very strong atmospheric water vapor transport [usually measured as vertically integrated vapor transport (IVT)], moving as much water as is discharged by the Amazon River (Zhu and Newell 1994, 1998). Consequently, when they impinge

[a] Current affiliation: European Centre for Medium-Range Weather Forecasts, Reading, United Kingdom.

Corresponding author e-mail: Francina Dominguez, francina@illinois.edu

DOI: 10.1175/JCLI-D-16-0386.1

on the orographic barriers of the U.S. West Coast, ARs can cause extreme precipitation and floods (Ralph et al. 2004, 2006; Neiman et al. 2008b; Ralph and Dettinger 2011; Dettinger et al. 2011; Neiman et al. 2011). In western Washington, for example, most flooding events observed in four watersheds were associated with ARs (Neiman et al. 2011). While the maximum AR frequency occurs on the northern coast of Oregon and Washington and gradually decreases southward (Rutz et al. 2014), ARs are still associated with some of the largest floods along watersheds in the California coast, such as the Russian River basin (Ralph et al. 2006). Also, 3-day precipitation totals associated with long-duration landfalling ARs in California are as large as anywhere in the country, including precipitation due to landfalling tropical storms and hurricanes (Ralph and Dettinger 2012). At the basin scale, the precipitation totals and resulting hydrologic response of the basins depend on the angle of impingement of the ARs in relation to the local topography (Ralph et al. 2003). Analyzing the basin hydrologic response in western Washington, Neiman et al. (2011) found that the basins draining the western slopes of mountains are impacted by westerly ARs, whereas basins draining the southern flanks had their largest discharges during southwesterly AR flows.

AR events involve a multiscale chain of events: from planetary-, synoptic-, and mesoscale to the watershed and river reach scale. As an example, an extreme AR event analyzed by Ralph et al. (2011) involved several key ingredients from the planetary scale (tropical convection, storm tracks) to the mesoscale (frontal wave). However, while extratropical cyclones (and ARs associated with these cyclones) usually develop with baroclinic instability as a lower- and upper-tropospheric coupled system, the connection between ARs and upper-troposphere atmospheric dynamics and variability has only recently become an active area of research. Of particular relevance is the effect of large-scale Rossby wave breaking (RWB) on meridional moisture transport and ARs. Liu and Barnes (2015) found that about 61% of the total extreme meridional moisture transport across 60°N was due to RWB events likely associated with ARs. Ryoo et al. (2013) linked the U.S. West Coast winter precipitation with upper-tropospheric potential vorticity (PV) during El Niño and La Niña years, through the interannual variability between the two regimes of RWB.

RWB represents irreversible mixing of the synoptic eddies in the midlatitude Rossby waves and has two primary regimes: anticyclonic wave breaking (AWB) and cyclonic wave breaking (CWB) (Thorncroft et al. 1993). AWB is often observed on the equatorward flank of the jet where conditions are dominated by anticyclonic wind shear, whereas CWB generally occurs on the poleward flank of the jet where cyclonic wind shear is predominant. During the mature stage of the two life cycles, both RWB types exhibit strong nonlinear characteristics. Analysis of eddy meridional momentum and vertical heat fluxes of the AWB suggests poleward momentum transport and "absorption" of eddy energy in the upper-tropospheric subtropics, which convert eddy kinetic energy (EKE) into stronger upper-tropospheric westerlies. In contrast, EKE accompanying the CWB is absorbed less because most of the upward propagating Rossby waves are reflected back downward from the high-latitude upper troposphere. As a result, the CWB has a relative persistent EKE. The feedback between eddies and the mean flow also results in a poleward shift of the jet after AWB but an equatorward shift of the jet after CWB. Associated with significantly different dynamic features, AWB (CWB) phenomena are manifested by irreversible mixing of PV in an anticyclonic (cyclonic) manner (McIntyre and Palmer 1985; Thorncroft et al. 1993).

In addition to eddy momentum and heat fluxes, moisture flux characteristics accompanying RWB are often discussed in the context of ARs. Close relationships have been found between the strongest landfalling ARs on the West Coast and clear AWB signals in the eastern Pacific (Payne and Magnusdottir 2014; Mundhenk et al. 2016b). A trajectory study by Ryoo et al. (2015) relates the different patterns of trajectories among ARs with RWB and demonstrates that about 66% of the AR events they evaluated are associated with AWB. While these studies demonstrate the importance of AWB, it is important to note that AR precipitation has the most significant impacts on the southwestern coast when CWB occurs more frequently over the eastern Pacific during El Niño years (Ryoo et al. 2013). In addition, the trajectory study by Ryoo et al. (2015) ties ARs with intense precipitation over the southwestern United States with a stronger relevance to CWB.

ARs are modulated by extratropical circulation patterns that are, in turn, related to RWB patterns. In fact, the latitude of maximum AR occurrence is related to that of maximum AWB occurrence (Mundhenk et al. 2016a). For this reason, changes in RWB can be used as indicators for AR variability and change (Payne and Magnusdottir 2014; Mundhenk et al. 2016b). As an example, El Niño–Southern Oscillation (ENSO) can modify storm track strength and location (e.g., storm track strength and location; Seager et al. 2003; Orlanski 2005; L'Heureux and Thompson 2006) and produce significantly different precipitation patterns over the West Coast, likely through ARs with different RWB types (Cayan and Roads 1984; Ryoo et al. 2013). In terms of long-term climatic trends, global warming can

potentially induce changes in RWB dynamics and consequently lead to changes in ARs. A poleward displacement of midlatitude jets with climate change is found to result in a robust and significant reduction of CWB frequency and a poleward shift of AWB distribution (Barnes and Hartmann 2012). The poleward shift of midlatitude jets also leads to a significant decrease of AR events in aquaplanet simulations (Hagos et al. 2015). At the same time, the thermodynamic change associated with climate change further complicates the problem (Gao et al. 2015). Such changes could potentially have a significant impact on regional precipitation in the West Coast (Salathé 2006; Dettinger 2011; Mass et al. 2011; Ryoo et al. 2013). This is particularly important because of the socioeconomic and ecologic consequences of changes in flood risk and water resources associated with these extreme events on both the local and regional scales. However, establishing the relationship between upper-tropospheric dynamics and regional hydrologic impacts is a critical first step before evaluating possible changes in regional hydrologic impacts due to climate change along the West Coast.

In this study, we focus on establishing the link between RWB and the regional-scale hydrological impacts of ARs on the U.S. West Coast, as a necessary step to bridge large-scale atmospheric dynamics and regional-scale hydrological variability. This understanding provides the dynamic basis for studies on changes in AR-related hydrologic impacts due to climate variability and change. To do this, we examine the AR characteristics along the U.S. West Coast in association with RWB. We make particular efforts on establishing the relationship between AR features and precipitation along the northwest and southwest coast of the United States, and quantifying the AR impact on two river basins within the northwest and southwest coast, respectively. Both of the basins have experienced severe AR-related floods in the past. In addition, we analyze the streamflow features of three additional river basins located between them. The key questions we want to address are these: 1) How important is RWB for the impacts of landfalling ARs on the U.S. West Coast? 2) Is there a significant precipitation difference associated with AWB- and CWB-ARs and how does it change with latitude? 3) How do coastal watersheds along a latitudinal gradient respond hydrologically to AWB- and CWB-ARs at a regional scale?

2. Data and methods

We examine the ARs that affect the U.S. West Coast with their eastern leading edges reaching 36°–49°N (black hatched area in Fig. 1a). Note that ARs at latitudes lower than 36°N were excluded in this analysis because of the small number of AR events and weak RWB signals (Fig. 2). To determine the importance of RWB for the impacts of landfalling ARs (question 1), we quantify the number of AR events and the precipitation associated with RWB. To explore the latitudinal variation of AR characteristics and impacts (questions 2 and 3), we examine two subsets of ARs reaching two 5° bands: 44°–49°N and 36°–41°N (red hatched grids in Fig. 1a). These two bands correspond to the northwest and southwest coasts of the United States.

We link the latitudinal variation of RWB-AR features, together with mountain range orientations, to local precipitation of two river basins. For the ARs impacting the northern band, we focus on the Chehalis River basin in western Washington (Fig. 1b) where several AR-induced major floods have caused extensive damages and economic losses. For instance, during 1–3 December 2007, the Chehalis basin experienced heavy rainfall and severe flooding, which caused a 4-day closure of the I-5 highway (Hayes 2008). The Chehalis basin is surrounded by mountains, except for the Pacific Ocean on its western boundary. Storms centered over the mountains on the southern Willapa Hills and Cascade foothills on the east can cause flooding in the upper Chehalis. Storms over the Olympic Mountains to the north can cause flooding in the lower Chehalis, without having much effect in the upper basin (Ruckelshaus Center 2012). For the ARs affecting the southern band, we focus on the Russian River basin in northern California (Fig. 1c). The effect of ARs on extreme flooding in the Russian basin has been studied by Ralph et al. (2006, 2013). All seven extreme streamflow events between 1997 and 2006 were found to be associated with ARs (Ralph et al. 2006). Surrounded by coastal mountains, the Russian River flows southward along the valley for about 145 km and drains into the Pacific Ocean (Anders et al. 2011). The mean orientation of the crest of the coastal mountains is along ~140°–320° (Ralph et al. 2013).

In addition to the Chehalis and Russian basins, we analyzed three additional coastal river basins along a latitudinal gradient between the Russian and Chehalis. The three additional river basins, from north to south, are the Willamette (northwestern Oregon), Rogue (southwestern Oregon) and Eel (northern California) basins. They are generally bounded by the Cascade/Sierra Nevada Mountains to the east and Pacific to the west, with rivers flowing into the Pacific Ocean. Using these five basins, we can assess the large-scale hydrologic impacts at different latitudes, while retaining the catchment-specific implications.

a. *MERRA data*

We use 30 years (1979–2009) of the National Aeronautics and Space Administration (NASA) Modern-Era

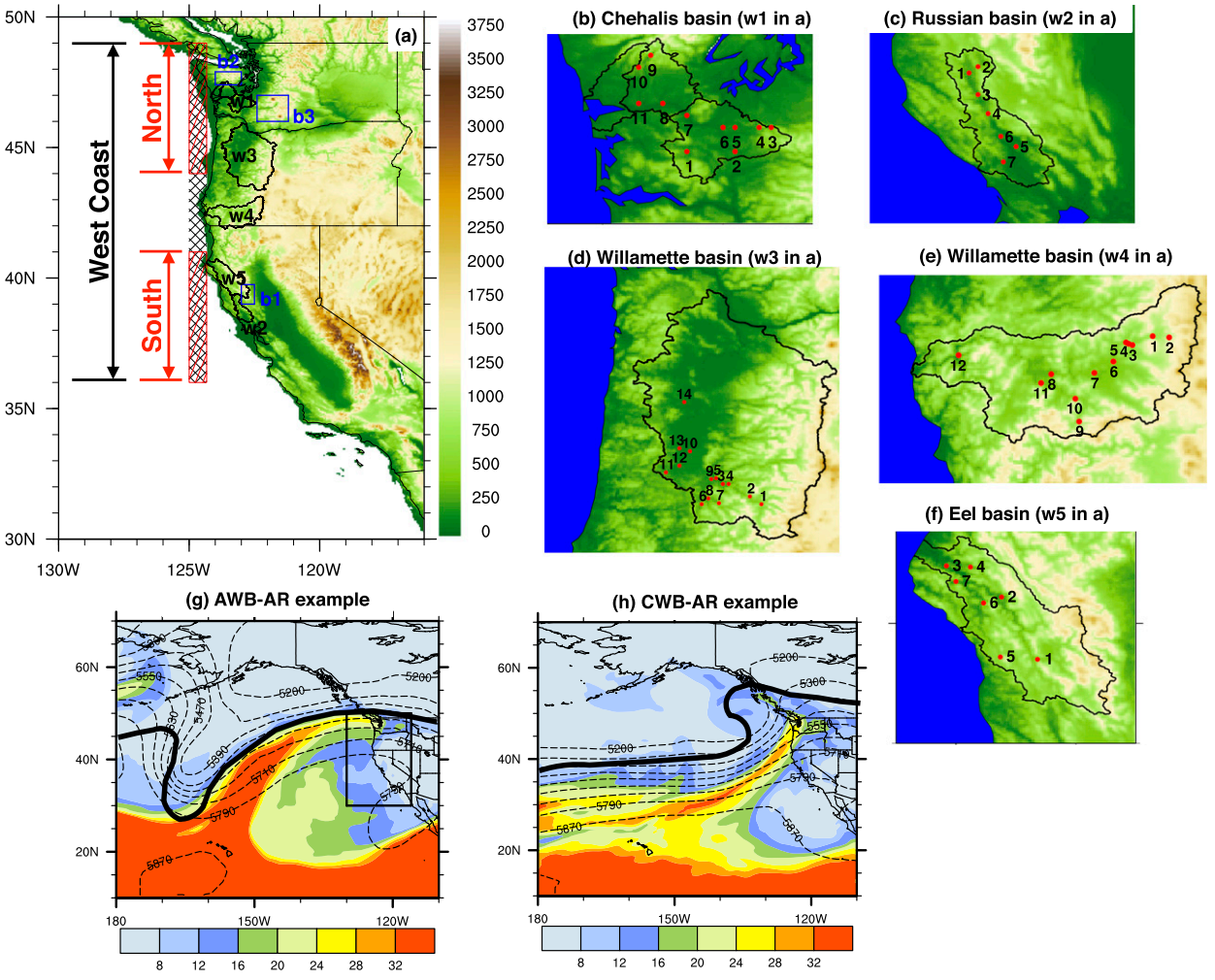

FIG. 1. (a) Topography features of the U.S. West Coast (unit: m). ARs with the leading edges reaching the black-hatched area are grouped as ARs affecting the West Coast; ARs withe the leading edges within the north (south) red-hatched area are grouped to represent the ARs affecting the northwest (southwest) coast. The five river basins are delineated by black lines and named w1–w5. Blue boxes suggest the area used to represent local precipitation features, named b1–b3. (b)–(f) Magnified view of the five basins w1–w5 with USGS streamflow gauges. (g) An AR example associated with AWB event on 22 Nov 1990, with precipitable water (color shaded, unit: kg m^{-2}) and 500-mb geopotential height (dashed contours, unit: m). (h) As in (g), but showing an AR event with CWB on 14 Jan 1988. The thick black lines in (g) and (h) indicate the 1.5-PVU contour at 350-K surface (1 PVU = 10^{-6} m^{-2} K kg^{-1}).

Retrospective Analysis for Research and Application (MERRA) reanalysis dataset for meteorological analysis. It has high resolution, both in time and space. MERRA is characterized by a significant improvement of the atmospheric branch of the hydrological cycle (Rienecker et al. 2011) compared with the previous generation of reanalyses (e.g., ERA-40, NCEP/NCAR-R1). Two-dimensional time-averaged fields (e.g., vertically integrated flux of specific humidity) are available at ½° × ⅔° and hourly resolution, and three-dimensional instantaneous fields (e.g., zonal wind) at pressure levels are available at 1.25° × 1.25° and 3-hourly resolution.

b. AR identification

The AR identification method developed by Lavers et al. (2012, 2013) is applied to MERRA data. In contrast to other detection methods that use satellite-estimated water vapor content to identify AR events (Ralph et al. 2004; Neiman et al. 2008a; Ralph and Dettinger 2012; Wick et al. 2013), Lavers et al. (2012) evaluate the AR dimensions using IVT values above a certain threshold according to the latitude range of the AR's leading edge. IVT is calculated using Eq. (1):

$$\mathrm{IVT} = \sqrt{\mathrm{QU}^2 + \mathrm{QV}^2}, \qquad (1)$$

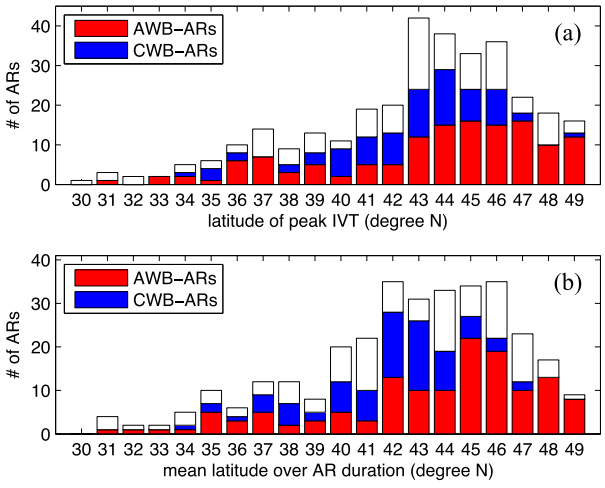

FIG. 2. Histograms of AR event numbers binned with (a) the impinging latitude at the time step with the maximum IVT and (b) the averaged impinging latitude with peak IVT over all steps within each AR's duration.

where QU and QV are the vertically integrated eastward and northward vapor flux respectively from MERRA.

We perform the AR detection algorithm three times by confining AR leading edges within three latitude bands. Two 5° latitude bands (44°–49°N and 36°–41°N) are selected to investigate differences in ARs with latitude, and one broad band (36°–49°N) is selected as the entire West Coast. As an example, the first step in the identification process for the AR events in the northern band (44°–49°N) is to determine the IVT threshold. The maximum IVT values for coastal grids (between 44° and 49°N along 124.7°W; northern red hatched area in Fig. 1a) at 1200 UTC of each day from October to March during 1979–2009 are taken to construct the distribution. Then, the IVT threshold is determined as the 85th percentile the IVT distribution. For each time step (hourly) during the 1979–2009 October–March period, the algorithm searches grids with IVT values above the threshold, starting from the coastal grids toward the west/southwest/south directions. A time step is flagged as an AR step if consecutive grids spanning more than 2000 km exceed the threshold. However, an AR event has to last more than 18 h (≥18 continuous AR step). We adjust the original length criteria used in Lavers et al. (2012, 2013) from 20 degrees of longitude to a solid length threshold of 2000 km to accommodate for our wider latitudinal range. In addition, individual events must be separated by at least 24 h. The IVT thresholds and the number of AR events for the three bands are shown in Table 1. We note that a lower threshold ($350\,kg\,m^{-1}\,s^{-1}$) is used when identifying AR events for the West Coast.

c. *RWB type classification*

RWB is manifested by the large-scale, rapid, irreversible overturning of PV contours on isentropic surfaces (McIntyre and Palmer 1985). An objective algorithm to detect RWB types developed by Strong and Magnusdottir (2008) is applied. This detection method objectively identifies the poleward-advection low-PV tongues associated with anticyclonically and cyclonically overturning PV contours at the 350-K isentropic surface (see Fig. 1 in Strong and Magnusdottir 2008).

In this study, PV is interpolated to the 350-K isentropic surface at every time step in which an AR event was detected. We then use the detection method of Strong and Magnusdottir (2008) to objectively classify RWB events as AWB and CWB. The detection method provides information about the location of each RWB. This information is used to link the RWB with the ARs. For the RWB to be linked to an AR, the location of RWB needs to be in the vicinity the concurring AR (within the box of 30°–70°N and 180°–110°W). In the case when more than one RWB occur simultaneously (e.g., Messori and Caballero 2015), the AR is attributed to the RWB type whose breaking location is closer to the AR. AR events can hence be classified into AWB-ARs, CWB-ARs, and nonbreaking ARs. Figures 1g and 1h show examples of AWB- and CWB-ARs with 1.5-PVU contours ($1\ PVU = 10^{-6}\,m^{-2}\,K\,kg^{-1}$).

RWB activity undergoes seasonal variation, and concentrating the RWB detection on a specific isentropic level could potentially limit the validity of the RWB detection. However, by examining the RWB signals on two more levels (340- and 330-K isentropic levels), we find consistent patterns of AR-related RWB detection with slightly different horizontal extension (not shown). Since the RWB type is more important than its horizontal

TABLE 1. Information about three latitude bands used to identify AR events and the number of AR events identified.

	Name	Latitudinal range	IVT threshold ($kg\,m^{-1}\,s^{-1}$)	Number of events		
				ARs	AWB-ARs	CWB-ARs
1	North 5° band	44°–49°N	384	192	80	61
2	South 5° band	36°–41°N	350	156	55	55
3	West Coast	36°–49°N	350	301	122	91

TABLE 2. Number of USGS streamflow gauges in the five coastal basins having record from 1979 to 2009.

	Basin name	No. of USGS streamflow gauges
1	Chehalis River basin	11
2	Russian River basin	7
3	Willamette River basin	14
4	Rogue River basin	12
5	Eel River basin	7

extent in this study, we take the results from 350 K as representative of RWB.

d. *Livneh gridded land surface data*

To investigate precipitation spatial distribution within the watershed, we use 1/16° latitude/longitude data from Livneh et al. (2013) for the winters from 1979 to 2009. The daily precipitation and temperature are derived from daily precipitation observations from approximately 20 000 NOAA Cooperative Observer Stations across the conterminous United States. We use this observational product to evaluate the spatial distribution of AR-related precipitation in sections 4 and 5.

e. *Streamflow gauge measurements*

The AR-related streamflow characteristics of the five river basins are obtained from long-term streamflow measurements by the U.S. Geological Survey (USGS). To be consistent, only gauges with 30-yr data availability (1979 October–2009 March) are included in our analysis. The numbers of streamflow gauges within each river basin are listed in Table 2 and their locations are indicated in Figs. 1b–f.

3. Importance of RWB-ARs to the West Coast

Using data and methods described in sections 2a–c, we identify AR events affecting the West Coast and classify those with clear RWB signatures into AWB or CWB types. A total number of 301 AR events are identified, and are binned based on the impinging latitude at the time of maximum IVT (Fig. 2a) and the average impinging latitude throughout AR duration (Fig. 2b), respectively. Consistent with previous studies (Neiman et al. 2008b; Rutz et al. 2014), the northwest coast experiences more ARs, especially to the north of 42°N. The number of ARs peaks at 43°–45°N (Fig. 2), in agreement with the peak AR probabilities found by Guan and Waliser (2015). Note that in Fig. 2 we include AR events that impinge south of 36°N. However, they are a small subset of events and usually accompanied by weak RWB signals, and thus are excluded in the rest of the analyses.

Among 301 AR events, about two-thirds of them (204 events) are associated with RWB. AWB-ARs (129 events) clearly outnumber CWB-ARs (75 events) from Table 1, consistent with the higher frequency of AWB in general as a result of the preferential equatorward propagation of Rossby waves and anticyclonic wind shear on the equatorward flank of the jets (Hoskins et al. 1977; Thorncroft et al. 1993; Nakamura and Plumb 1994; Peters and Waugh 1996; Barnes and Hartmann 2012). However, Ryoo et al. (2015) estimated that ~66% of ARs are associated with AWB. The discrepancy likely arises due to the difference in the AR detection method: IVT is used in this study but precipitable water was the criteria for Ryoo et al. (2015).

Figure 2 also suggests that peak IVT of CWB-ARs tends to occur at 40°–46°N whereas peak IVT of AWB-ARs impinges mostly at 42°–49°N. As a result, more frequent AWB-ARs are also found affecting the northern 5° band but similar AWB-ARs and CWB-AR frequencies are found in the southern 5° band (Table 1). However, within the confining latitude bands, some AR events of long duration and wide-range effect are counted twice (once in each latitude band). The summation of two subsets is thus larger than for the West Coast (Table 1). In fact, 28 CWB-ARs are counted in both latitudinal subsets while only 14 AWB-ARs are included in both subsets, indicating a broader north-to-south movement of CWB-ARs. AWB-ARs, on the other hand, appear to impinge at higher latitudes and have limited latitudinal movement within their lifespan.

In addition to the number of ARs related with RWB, we also examine their significance to winter precipitation. We quantify the precipitation associated to each AR using the 2-day maximum precipitation [the same approach used in Warner et al. (2012)], occurring ±2 days around the peak IVT time step. The ratio of RWB-ARs precipitation to the total AR precipitation is calculated and shown in Fig. 3. More than 70% of total AR precipitation results from RWB-ARs in Washington and the fraction gradually decreases to ~60% toward the southwest coast (Fig. 3a). However, mountainous regions in California have higher ratios. When partitioning the total ratios in Fig. 3a into AWB-ARs and CWB-ARs parts, they clearly demonstrate opposite spatial patterns (Figs. 3b,c). The northwest coast (Washington and Oregon) is predominantly affected by AWB-ARs, accounting for over 40% of AR precipitation, with even more on the Cascades (>45%). In contrast, a larger portion of AR precipitation in the southwest coast (California) is associated with CWB-ARs despite their peak IVT latitudes at 40°–46°N. The reasons for the large difference in the

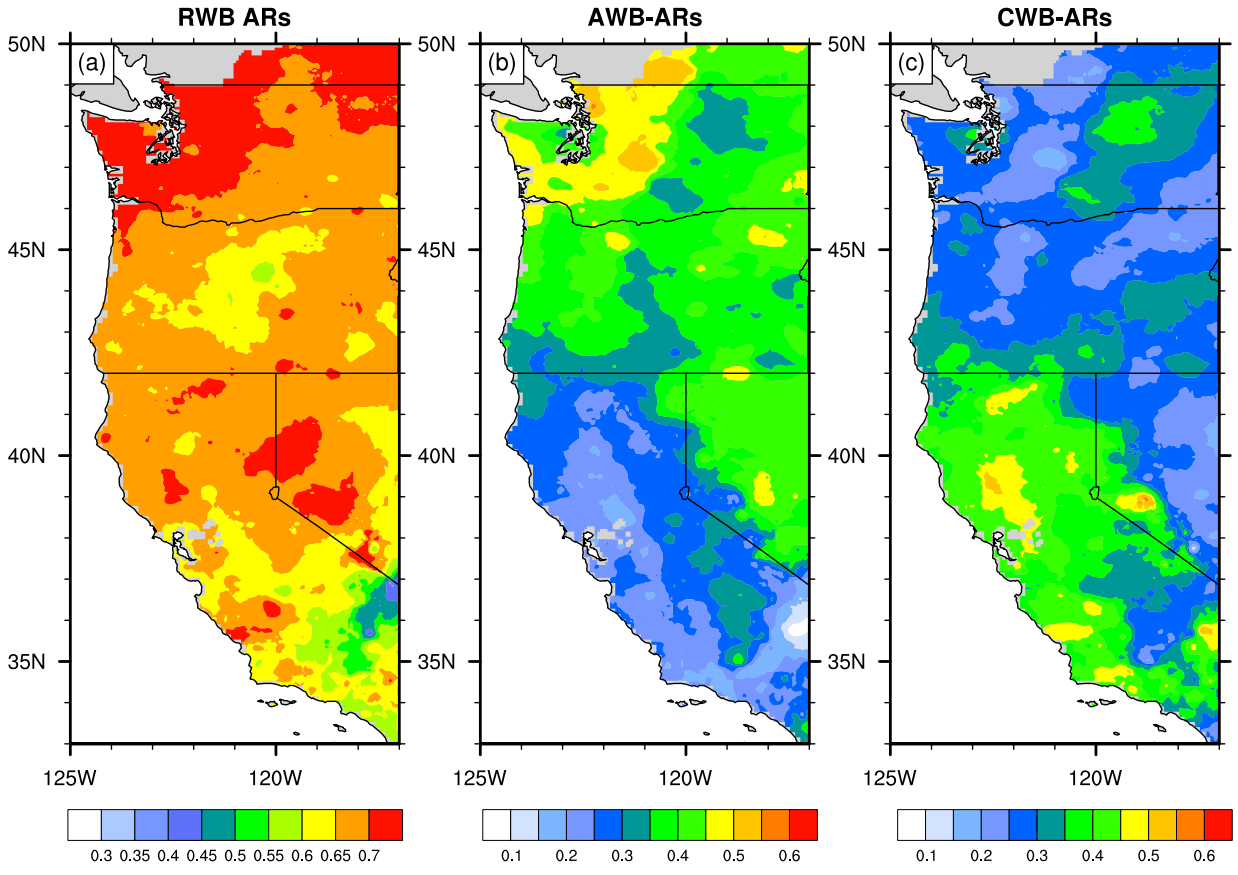

FIG. 3. Ratio of AR-related precipitation due to (a) RWB-ARs, (b) AWB-ARs, and (c) CWB-ARs.

region of impact between the two AR types are further explored by two subsets of ARs affecting the two latitude bands and river basins.

4. Difference of AWB and CWB AR features

To demonstrate the AR features associated with AWB and CWB, we analyze two subsets of ARs reaching the two 5° latitude bands. Instead of mixing all ARs impacting the West Coast together, we use two AR subsets because, by refining the ARs impinging the northwest (44°–49°N) and southwest coast (36°–41°N), we can 1) obtain clear AR features and 2) reveal the latitudinal variation of AR features with two RWB types.

a. Synoptic composites

AR synoptic composites are constructed for the north band (Figs. 4a–c) using MERRA data. Compared with composites averaged from all AR events (Fig. 4a), AWB-ARs appear to impinge in a more westerly direction (Fig. 4b). In contrast, CWB-ARs impinge in a southwesterly direction toward the coast (Fig. 4c). Note that we focus on the impinging angles of ARs toward the West Coast, but not the overall orientation of the filamentary structure. In fact, CWB-ARs have more zonal orientation off the coast, while AWB-ARs have a more meridional orientation, similar to the features found by Sodemann and Stohl (2013).

AWB-ARs are characterized by a pronounced 875-mb high to the southeast of the ARs while CWB-ARs show an enhanced 875-mb low to the northwest of the ARs (Figs. 4b,c). The near-surface low found in CWB-ARs is consistent with the single and large surface cyclones mostly coexisting with CWB-ARs (Moore et al. 2012; Sodemann and Stohl 2013). CWB-ARs are also associated with a longer filamentary structure with higher IVT ($\geq 560\,\mathrm{kg\,m^{-1}\,s^{-1}}$) (Fig. 4c). This could be partially attributed to the stronger wind speed of CWB-ARs (as seen the stronger pressure gradient for the 875-mb level in Fig. 4c). Similar synoptic features are found in the composites for the south-band subset (Figs. 4d–f) but with the patterns shifted southward. However, the strength of AWB-ARs along the southern coast is weakened significantly. Further details of the IVT transport and dynamical features will be investigated in section 4b,

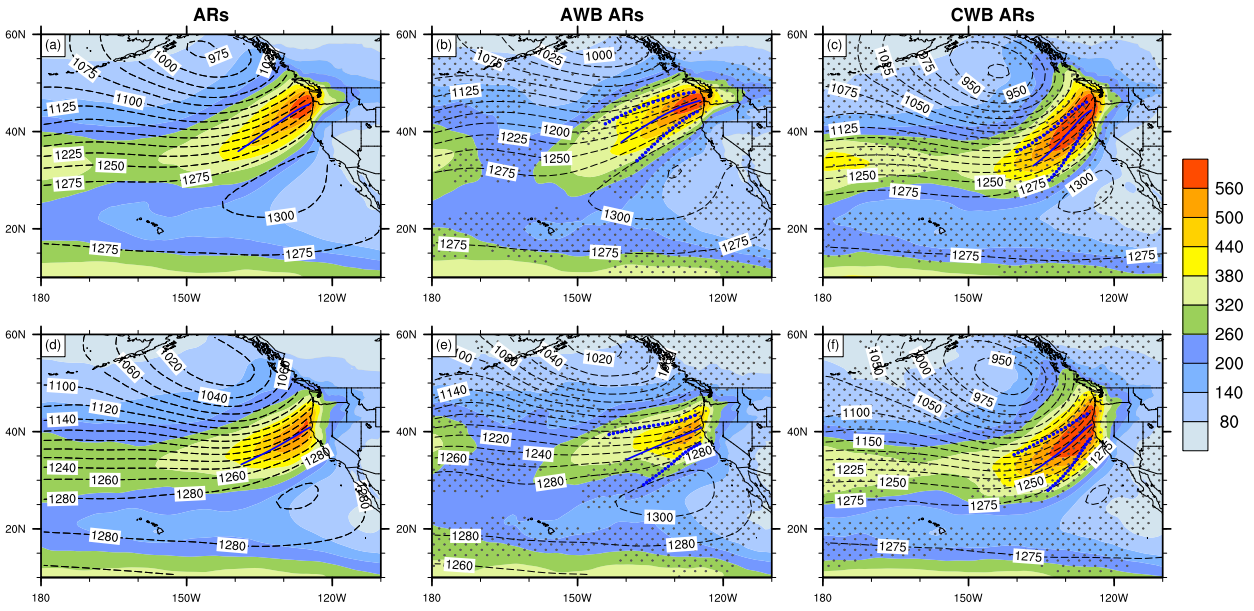

FIG. 4. Composites of IVT (color shaded, unit: kg m^{-1} s^{-1}) and 875-mb geopotential height (dashed contours, unit: m) for the (a)–(c) northern and (d)–(f) southern subset of ARs. Blue solid lines suggest the averaged IVT axes starting from the coast and extending 2000 km into the Pacific. The blue dots in (b),(c),(e), and (f) suggest the standard deviation of IVT axes.

to explain the difference between AWB- and CWB-ARs and the latitudinal variation.

A similar pattern as northern AWB-AR composites (Fig. 4b) with a strong high pressure to the southeast of the ARs is found by Neiman et al. (2008b) for ARs with water vapor plumes impacting the northwest coast. In contrast, CWB-AR composites (Figs. 4c,f) with an anomalous low to the northwest of the ARs resemble those for ARs affecting the southwest coast (see Fig. 6 in Neiman et al. 2008b). This suggests a significant and consistent role of AWB-ARs for the northwest coast, but a more prominent role of CWB-ARs for the southwest coast.

b. *Vertical structures*

Decomposing the IVT into moisture and wind components at each level, Fig. 5 shows the averaged vertical profiles near the coast for each AR type. They are extracted from the grid along 124.7°W having the maximum IVT. Therefore, for the northern ARs, all the profiles (Figs. 5a–c) are from the grids in the north 5° band (the north red hatched area in Fig. 1a); for the southern ARs, profiles (Fig. 5d–f) are extracted from the grids in the south 5° band (the south red hatched area in Fig. 1a). Figure 5 clearly reveals that the horizontal wind speed is the dominant factor in driving the difference of IVT. For the northern ARs, CWB-ARs on average have stronger winds below 750-mb level, which result in significant stronger moisture transport below the 800-mb level despite slightly less humidity. However, the AWB-ARs have much stronger upper-tropospheric winds. A similar horizontal wind difference between AWB- and CWB-ARs is found in the southern ARs, but with greater moisture fluxes of CWB-ARs extending to 550 mb. The horizontal wind, especially the lower-tropospheric winds, generally decreases with latitude (Figs. 5a,d).

In addition to coastal profiles, we present the composite vertical cross sections along the core IVT axes (Fig. 6). Specific humidity and vertical and horizontal wind speed are shown along the 2000-km axes for each RWB type. Consistent with Fig. 5, CWB-ARs have stronger horizontal winds in the lower troposphere, extending to ~1500 km off the coast (Figs. 6c,g). It is consistent with the enhanced pressure gradient of CWB-ARs suggested by Fig. 4. Humidity, on the other hand, shows smaller differences close to the coast and larger differences away from the coast (Figs. 6d,h). The reason is that 2000 km away from the coast, along the CWB-AR axes, the AR is usually located at lower latitudes than AWB-ARs (Figs. 4c,f).

The vertical wind component, critical in producing precipitation, is plotted in Fig. 6. Significant stronger uplifting by CWB-ARs is found from the coast to ~1500 km offshore between 900 and 200 mb. Taking a plan view of the vertical winds at 750 mb where the maximum occurs, AWB-ARs show strong uplifting confined closely to the coast (blue shading, Fig. 7b), indicating a stronger relation with orographic lifting near the coast. CWB-ARs, on the other hand, show greater and extended regions of uplift offshore (blue

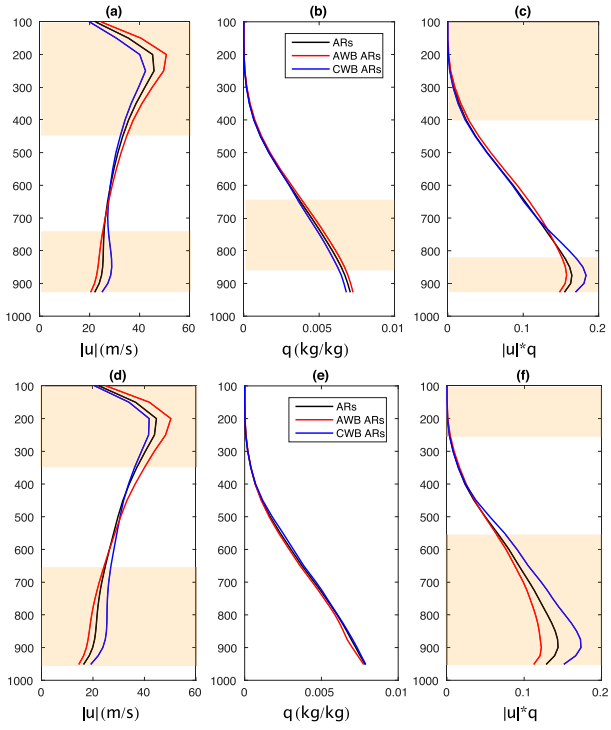

FIG. 5. Vertical profiles composites for the (a)–(c) northern and (d)–(f) southern subset of ARs. Orange shaded levels are the levels with significant different means between AWB- and CWB-ARs with 99% confidence level.

shading, Figs. 7c,f). It has been shown that vertical heat fluxes are much stronger in the mature phase of CWB, as most upward EKE is reflected in CWBs rather than absorbed, as in the AWB case (Thorncroft et al. 1993). This helps support the stronger vertical wind component shown in CWB-ARs. Moreover, the extended region of ascent could also be attributed to the stronger wind–terrain interaction of CWB-ARs, due to the stronger lower-tropospheric winds, which tend to extend the upstream ascent significantly (Wang and Chang 2012). It is also important to note that AWB-ARs have additional local maxima of uplifting over the mountains farther inland, over the Cascades in Fig. 7b and over the Rockies in Fig. 7e.

In the upper troposphere, AWB-ARs have a more poleward displacement of the jet than CWB-ARs (Figs. 7g–l). AWB-ARs occur on the equatorward flank of the jet where anticyclonic wind shear is present; AWB also helps maintain the poleward position of the jet through poleward momentum fluxes. On the other hand, CWB-ARs occur on the poleward flank of the jet and the jet location is maintained relatively equatorward. However, the southern AWB-ARs are much weaker than the northern AWB-ARs (as can be seen in Figs. 7h,k) because they are associated with weaker westerly winds and probably are subject to stronger EKE absorption by the upper subtropics as moving closer to the subtropics.

c. *Impinging angles and precipitation distribution*

Given the orographic uplifting suggested in section 4b, we connect the AR impingement toward the coast with precipitation inland. We calculate the impinging angle of ARs to the coast, based on the direction of vapor flux at the grid with maximum IVT along 124.7°W (red hatched area in Fig. 1a). We define the impinging angle as the angle between the IVT vector and the meridian (see the schematic in Fig. 8). The difference in impinging angles (averaged over the lifespan of the ARs) between AWB- and CWB-ARs, is represented by the histograms of impinging angles in Fig. 8. The averaged variation of impinging angles within the AR's lifespan is ±10.0° for the northern subset of ARs and ±11.5° for the southern subset of ARs relative to the averages over the lifespan.

For the north band, the angles of CWB-ARs mostly range between 10° and 46°, while AWB-ARs have a broader range and have a median angle of 55.1°. Because of the crucial interaction between AR and topography (Ralph et al. 2003; Neiman et al. 2011), the impinging angle differences associated with these two types of ARs result in a very distinct area of topographic uplifting and thus peak precipitation. AWB-ARs, with more westerly impinging angles, result in positive precipitation anomalies over the Cascades (Fig. 9b); meanwhile, CWB-ARs, with more southwesterly impingement, contribute mostly to the precipitation over the Olympics (Fig. 9c). It is clear from these results that intense precipitation preferentially occurs over mountains where ARs impinge orthogonally (indicated by the sketched lines in Figs. 9b,c). Here we assume the impinging angles toward the mountains are very similar to the angles toward the coast, neglecting the local deflection of winds.

In a previous study, Neiman et al. (2011) analyzed four basins in western Washington and constructed composites based on the top 10 extreme events for each basin. The precipitation patterns for the Green River basin located on the western slope of the Cascades and the Satsop River basin draining the southern flank of the Olympics (see Fig. 9 in Neiman et al. 2011) resemble Figs. 7b and 7c, respectively. It is reasonable to infer that AWB-ARs are likely to contribute to the top events measured at the site on the western flank of the Cascades (in the Green basin) while CWB-ARs tend to produce extreme conditions for the site draining the southern Olympics (in the Satsop basin). In fact, referring to their composites of IVT and

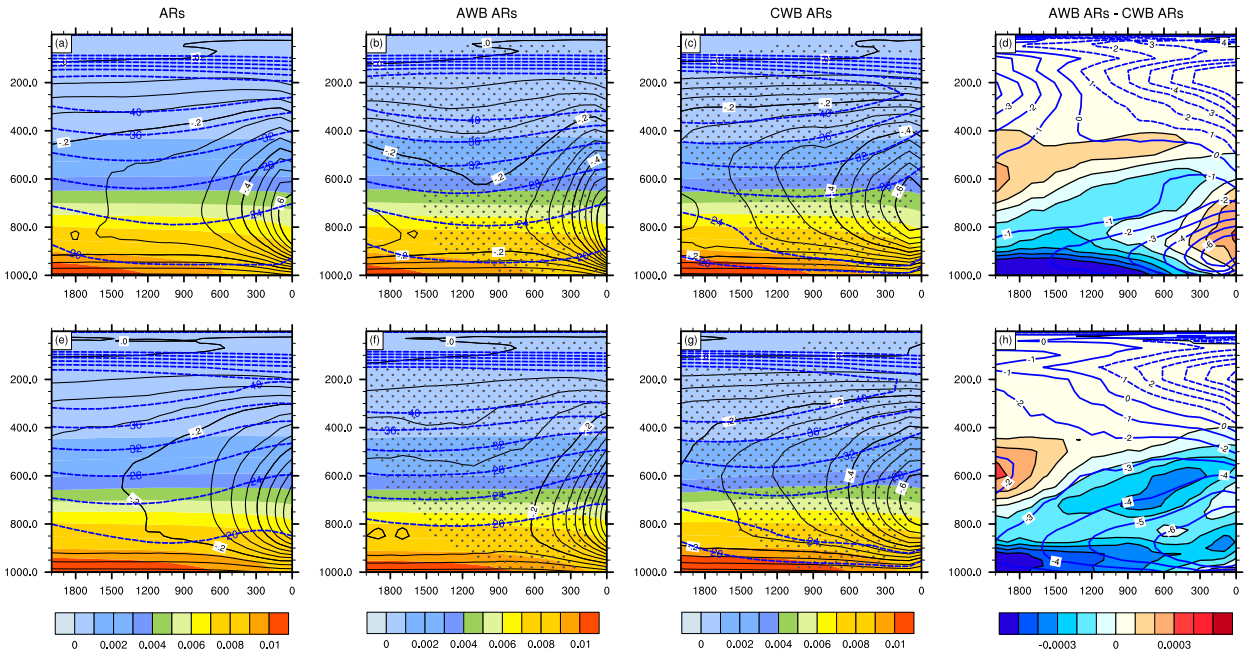

FIG. 6. Vertical cross sections composites along the AR maximum IVT axes for the (a)–(c) northern and (e)–(g) southern subset of ARs. Specific humidity (unit: kg kg^{-1}) is shaded by colors; omega (unit: Pa s^{-1}) is contoured by black lines with intervals of 0.05 Pa s^{-1}; wind speed (unit: m s^{-1}) is contoured by blue dashed lines with intervals of 4 m s^{-1}. Stippled areas in (b),(c),(f), and (g) show regions with significant different omega means between AWB- and CWB-ARs with 90% confidence level. (d),(h) The difference of specific humidity (color shaded) and wind speed (blue contours) between AWB-ARs and CWB-ARs for the northern and southern ARs, respectively. Horizontal tick label indicates the distance (unit: km) away from the coast into the Pacific. Each column shares the same color bar.

near-surface geopotential heights (Figs. 10 and 12 in Neiman et al. 2011), they show the characteristic features of AWB- and CWB-ARs (Figs. 4b,c).

A similar relationship between precipitation and AWB- and CWB-AR impinging angles holds for the south-band ARs (Fig. 8b), yet with a limited number of AWB-AR events. However, AR-related precipitation in the south band is dominated by CWB-ARs. Positive precipitation anomalies over the Sierra Nevada and other coastal mountains due to CWB-ARs are clearly shown in Fig. 9f. As the mountains are oriented along ~140°–320° (Ralph et al. 2013), CWB-ARs impinging at ~25°–50° arrive more orthogonally with respect to the topographic barrier. Furthermore, CWB-ARs are associated with much higher IVT than AWB-ARs (Fig. 5), a phenomenon amplified for the southern ARs.

5. Hydrological impacts on river basins

The spatial precipitation distribution corresponding to different AR impingement angles can significantly impact the river basin response. In this section, we place particular emphasis on extreme events. First, we investigate how the local precipitation features of two river basins (Chehalis and Russian) within the north and south 5° bands are related with impinging angle and IVT features accompanying RWB-ARs. Second, we quantify the relationship of AWB- and CWB-ARs to the extreme streamflow events in the five river basins along the West Coast.

a. *Precipitation in relation to impinging angle and IVT*

For the northern ARs (impinge between 44° and 49°N), AWB-ARs result in maximum precipitation over the Cascades whereas CWB-ARs result in maximum precipitation over the Olympics (Fig. 9). They both affect the Chehalis basin because the western Cascades drain to the upper Chehalis and the southern Olympics drain toward the lower Chehalis. We thus select the two boxes (b1 and b2 in Fig. 1a) over the western Cascades and the southern Olympics, and use 2-day averaged precipitation (averaged for all grids from Livneh gridded precipitation data within each box) of each AR event to establish the relationships between precipitation, impinging angle and IVT (averaged over the lifespan of the ARs; Figs. 10a–d).

Extreme precipitation events over the western Cascades are mostly associated with AWB-ARs, especially those with impinging angles between 40° and 80° (Fig. 10a). CWB-ARs, having <50° impinging angles, show an increasing precipitation trend with

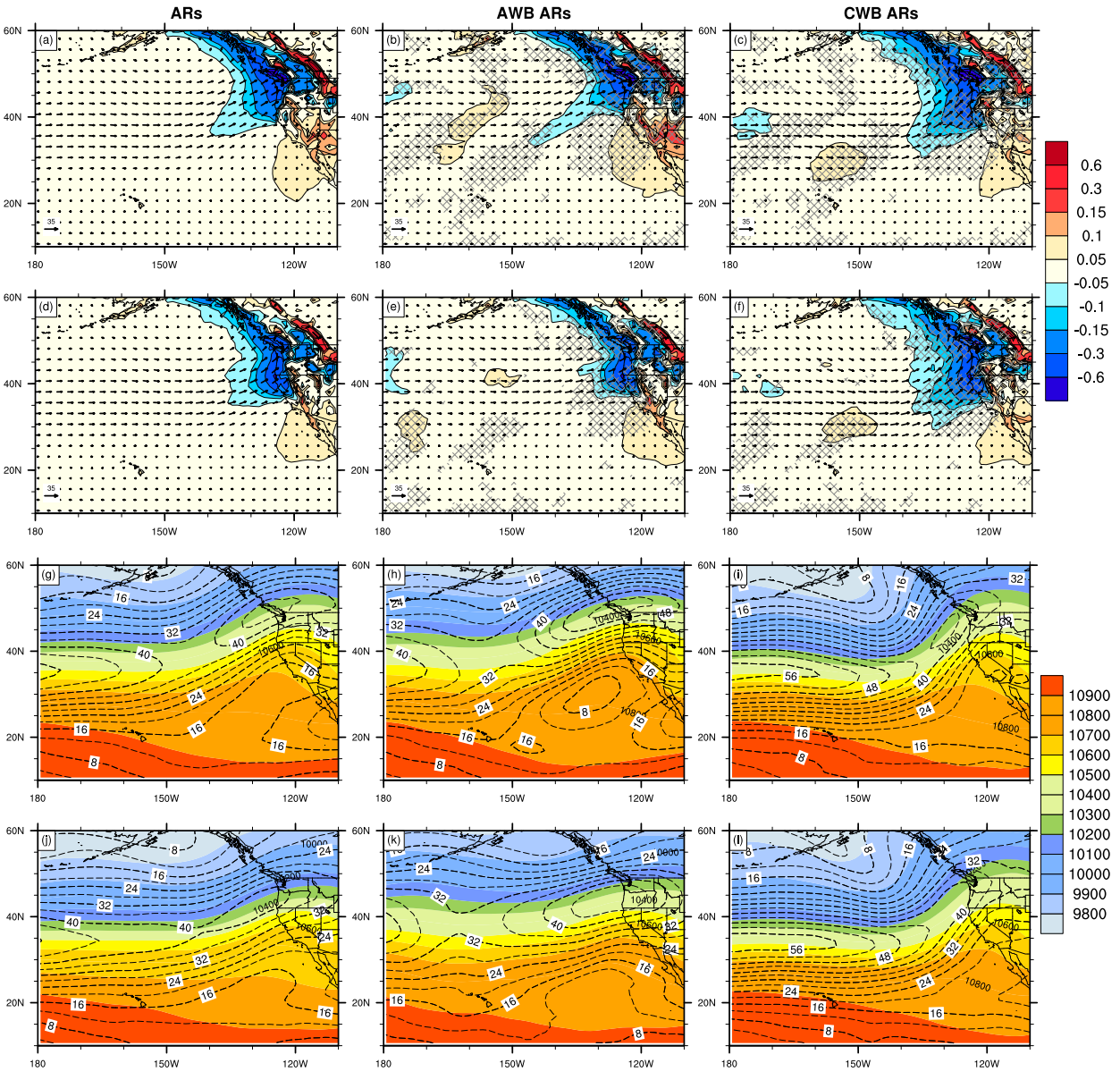

FIG. 7. Omega (color shaded, unit: Pa s^{-1}) and horizontal wind (vectors, unit: m s^{-1}) composites at 750-mb level for the (a)–(c) northern and (d)–(f) southern subset of ARs. Also shown are geopotential height (color shaded, unit: m) and horizontal wind speed (dashed contours, unit: m s^{-1}) composites at the 250-mb level for the (g)–(i) northern and (j)–(l) southern subset of ARs. Hatched areas in (b),(c),(e), and (f) show regions with significant different omega means between AWB- and CWB-ARs with 90% confidence level.

increasing impinging angle as it becomes more orthogonal toward the Cascades. In terms of IVT, both AWB- and CWB-ARs suggest a positive correlation between IVT strength and precipitation intensity (Fig. 10b). However, the slope of AWB-ARs is larger than CWB-ARs, suggesting more efficient transformation of water vapor into precipitation accompanying AWB-ARs with favorable impinging angles. An orthogonal impingement toward the Cascades requires an impinging angle of 90°–100° (see angle definition in Fig. 8), which is different from the 40°–80° range we see in Fig. 10a. Cases with impinging angles of 90°–100° tend to have lower humidity and thus weaker IVT (not shown), as they have advection from higher latitude and drier conditions. Therefore, while impinging angles could be a limiting factor for IVT when exceeding 90°, more southerly impingement and a stronger IVT (like the ones with CWB-ARs) does not guarantee extreme precipitation over the western Cascades because they are less orthogonal to the mountains.

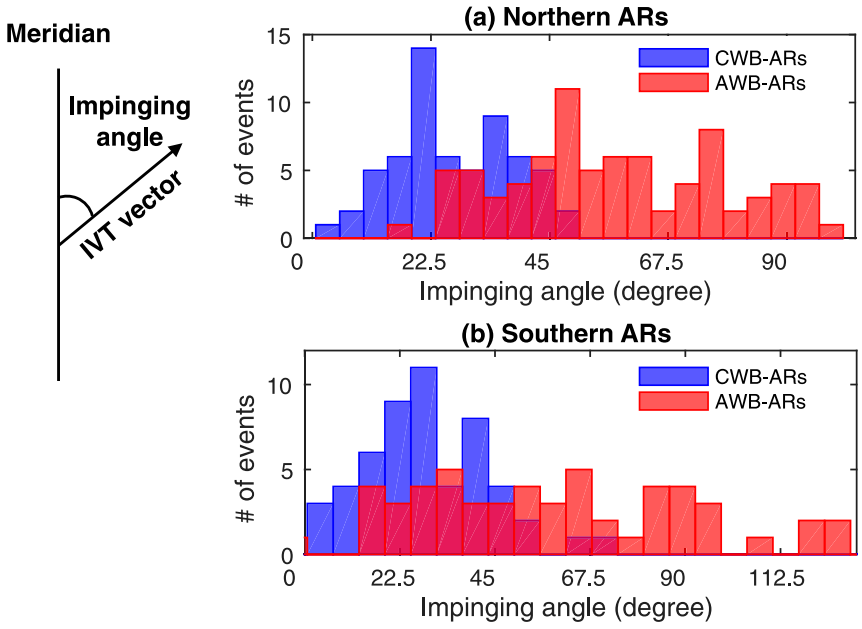

FIG. 8. Histograms of AR impinging angles for the (a) northern and (b) southern subset of ARs. The schematic on the left suggests the definition of impinging angles.

Over the southern Olympics, however, the majority of the extreme precipitation cases can be attributed to CWB-ARs (Fig. 10c) with ~35° of impinging angle. In this case, CWB-ARs have a higher efficiency in transforming water vapor into precipitation with a slightly steeper slope between precipitation intensity and IVT (Fig. 10d) than AWB-ARs. The difference between the slopes is not large probably due to the fact that AWB-ARs also produce large amounts of precipitation over the southwestern Olympics.

Similar analysis is repeated for the southern ARs (impinge between 36° and 41°N) on the Russian River basin by selecting a box over its upstream mountains (b3 in Fig. 1a). We find that CWB-ARs are predominantly contributing to the extreme precipitation events. CWB-ARs generally have impinging angles less than 50° and those events that induce the most intense precipitation have an average impinging angle of ~40° (Fig. 10e). However, in this case CWB-ARs have a much steeper slope between IVT and precipitation intensity than AWB-ARs (Fig. 10f), indicating the important role of impinging angle on modulating the AR landfall. Moreover, AWB-ARs generally have weaker IVT, which is consistent with weaker westerly winds moving equatorward and likely associated with weaker EKE.

b. *Extreme streamflow*

Finally, we investigate the role of the two RWB-AR types on the most extreme streamflow events for five basins along the West Coast. For each river basin, the top 20 AR-related streamflow events for the 30-yr period (1979 October–2009 March) are selected and attributed to AWB- or CWB-ARs. As expected, the differences in precipitation intensity due to varying impinging angle (shown in sections 4c and 5a) are the key determinants of the AR type on extreme streamflow. For the Chehalis basin, it is shown that AWB-ARs play a predominant role (Fig. 11b) in explaining the top streamflow events measured within the basin. AWB-AR events are characterized by positive precipitation anomalies over the western Cascades and more efficient production of precipitation from IVT. However, it is also important to note that the number of CWB-ARs causing the top 20 extreme streamflow events measured at stations 8, 9, and 10 is substantial. These stations drain the southern flank of the Olympics, where positive precipitation anomalies are caused by CWB-ARs (see Figs. 9c and 10d).

In the Russian River basin, CWB-ARs are responsible for most of the extreme streamflow events (Fig. 11f). Enhanced precipitation results from CWB-ARs with orthogonal impingement on the coastal California mountains and strong IVT (Figs. 9f and 10f). CWB-ARs also result in significantly higher streamflow in the Russian basin than AWB-ARs (not shown) while the opposite is not found in the Chehalis basin.

Three additional basins—the Willamette, Rogue, and Eel basins, located between the Chehalis and Russian basins—show a clear transition of the dominant pattern from AWB-AR to CWB-AR on extreme streamflow events (Fig. 11). This latitudinal gradient is consistent

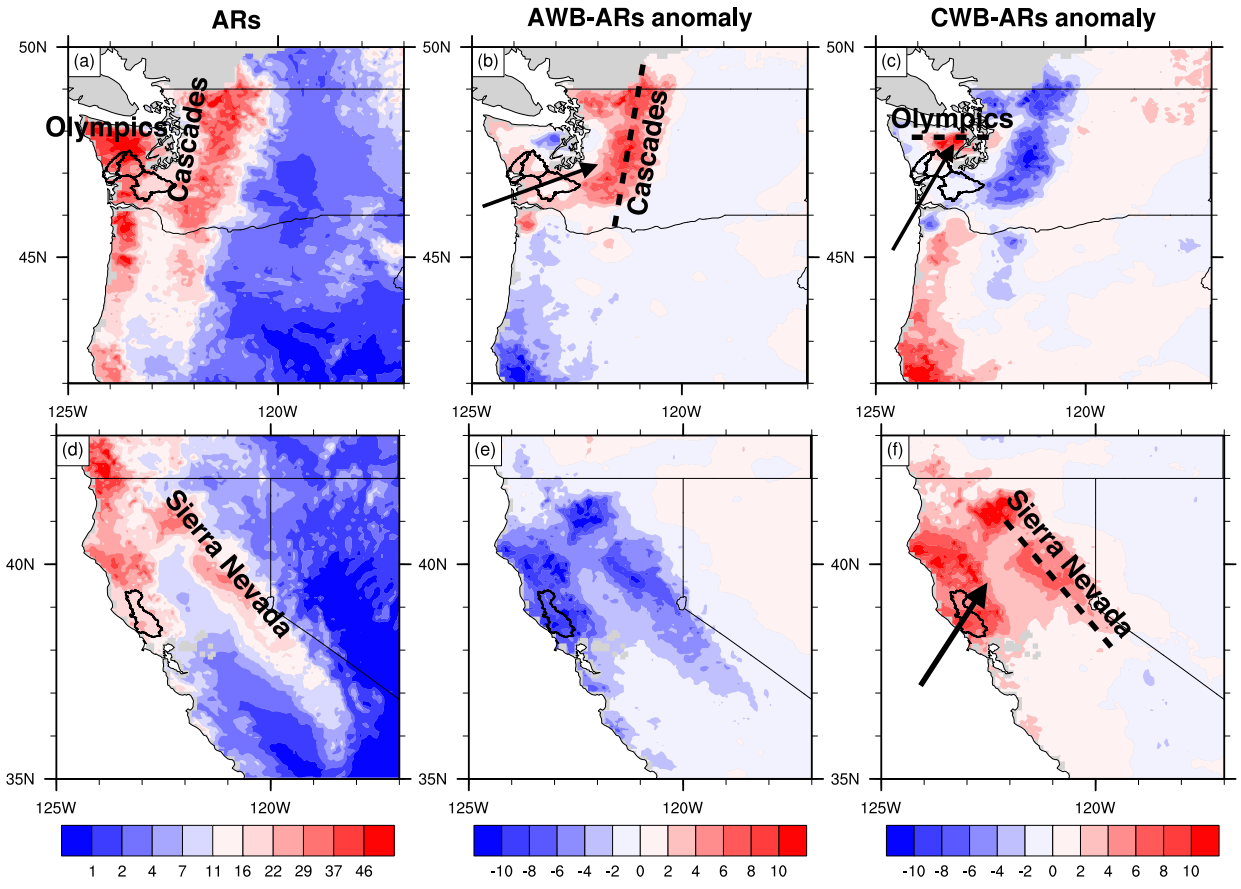

FIG. 9. (a) Composites of precipitation (converted to mm day^{-1}), (b) AWB-AR precipitation anomalies (unit: mm day^{-1}) and (c) CWB-AR precipitation anomalies (unit: mm day^{-1}) for the northern subset of ARs. (d)–(f) As in (a)–(c), but for the southern subset of ARs. The dashed lines suggest he orientation of the mountains, and the arrows suggest the inland impingement of AWB- and CWB-ARs.

with the north–south precipitation transition shown in Fig. 3. The coastal mountains generally shift from north–south orientation in western Washington to northwest–southeast orientation in northern California, which favors a more orthogonal impingement of CWB-ARs in the south. In addition, the CWB-ARs are able to maintain the IVT strength moving southward, producing enhanced precipitation during landfall and high streamflows along the southwest coast.

6. Summary and conclusions

In this work we bridge the large-scale, upper-tropospheric RWB dynamics with regional hydrological responses through ARs along the U.S. West Coast. Among the total number of AR events, about two-thirds are associated with RWB. The ratio remains the same for all ARs identified for the West Coast (36°–49°N), and two subsets of ARs that impact the northern and southern parts of the coast (36°–41°N and 44°–49°N). AWB-ARs tend to impinge at higher latitudes (>43°N) and have limited meridional movement within their life cycles. On the other hand, CWB-ARs can travel from high to low latitudes along the coast within their lifespan, likely due to the fact that CWB-ARs have more persistent EKE than AWB-ARs.

The synoptic features associated with AWB-ARs are characterized by a pronounced surface high to the southeast of the ARs, while CWB-ARs generally have an enhanced surface low to the northwest of the ARs. CWB-ARs are shown to have significant larger moisture transport in the lower-troposphere than AWB-ARs (shown schematically in Fig. 12), mainly attributable to stronger winds. The strengthened winds in the lower troposphere of CWB-ARs are observed from the coast to ~1500 km into the Pacific Ocean along the IVT axes. When compared to AWB-ARs, CWB-ARs show much broader regions of ascent, extending hundreds of miles away from the coast. This is consistent with the stronger vertical eddy heat fluxes seen in the mature stage of CWB. In

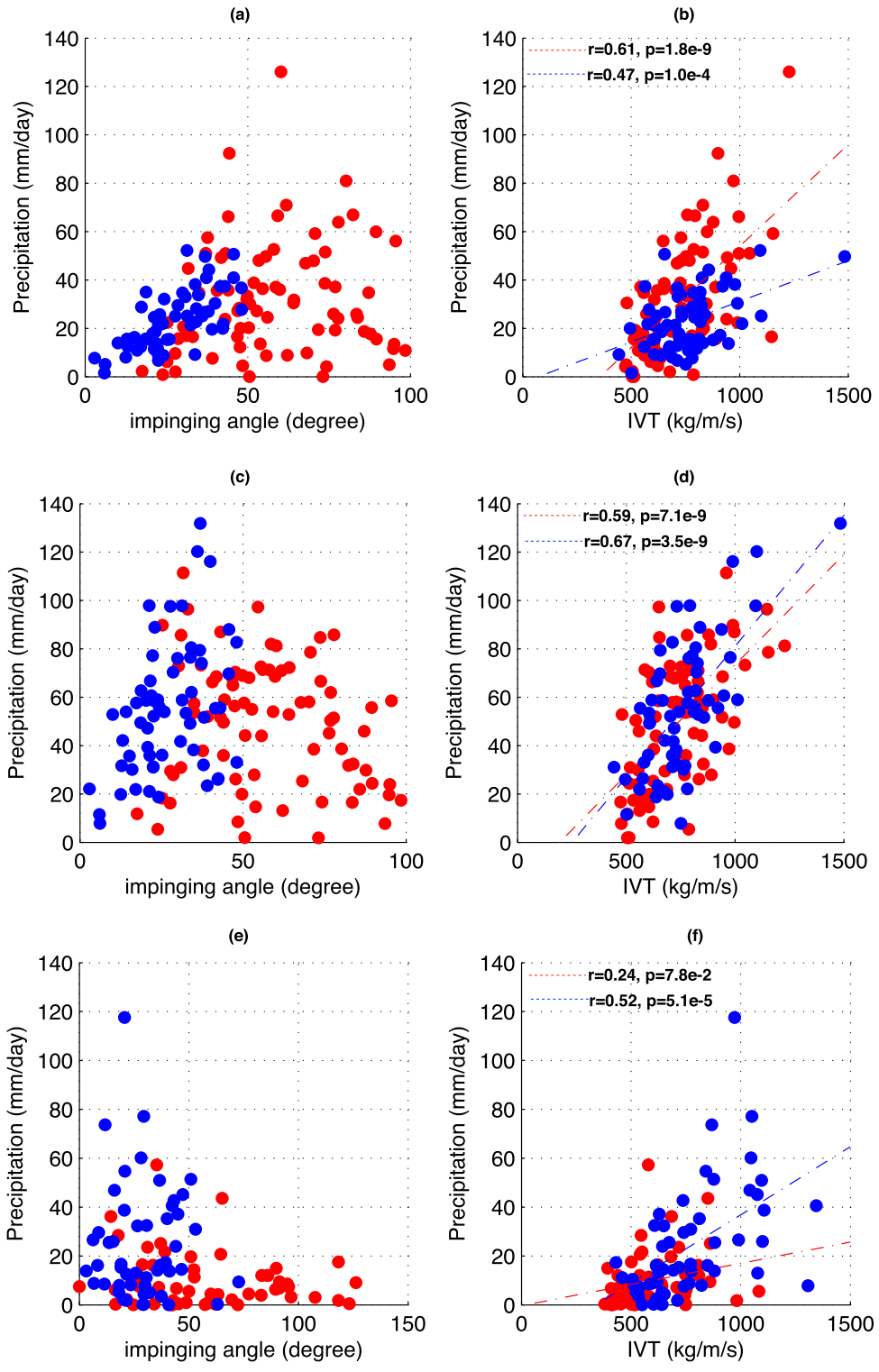

FIG. 10. Scatterplots of 2-day averaged precipitation (averaged over the three blue boxes in Fig. 1a; converted to mm day^{-1}) and AR impinging angles: (a) western Cascades (b1 in Fig. 1a), (c) southern Olympics (b2 in Fig. 1a), and (e) upstream Russian (b3 in Fig. 1a). Also shown are scatterplots of 2-day averaged precipitation (averaged over the three blue boxes in Fig. 1a; converted to mm day^{-1}) and AR IVT: (b) western Cascades (b1 in Fig. 1a), (d) southern Olympics (b2 in Fig. 1a), and (f) upstream Russian (b3 in Fig. 1a).

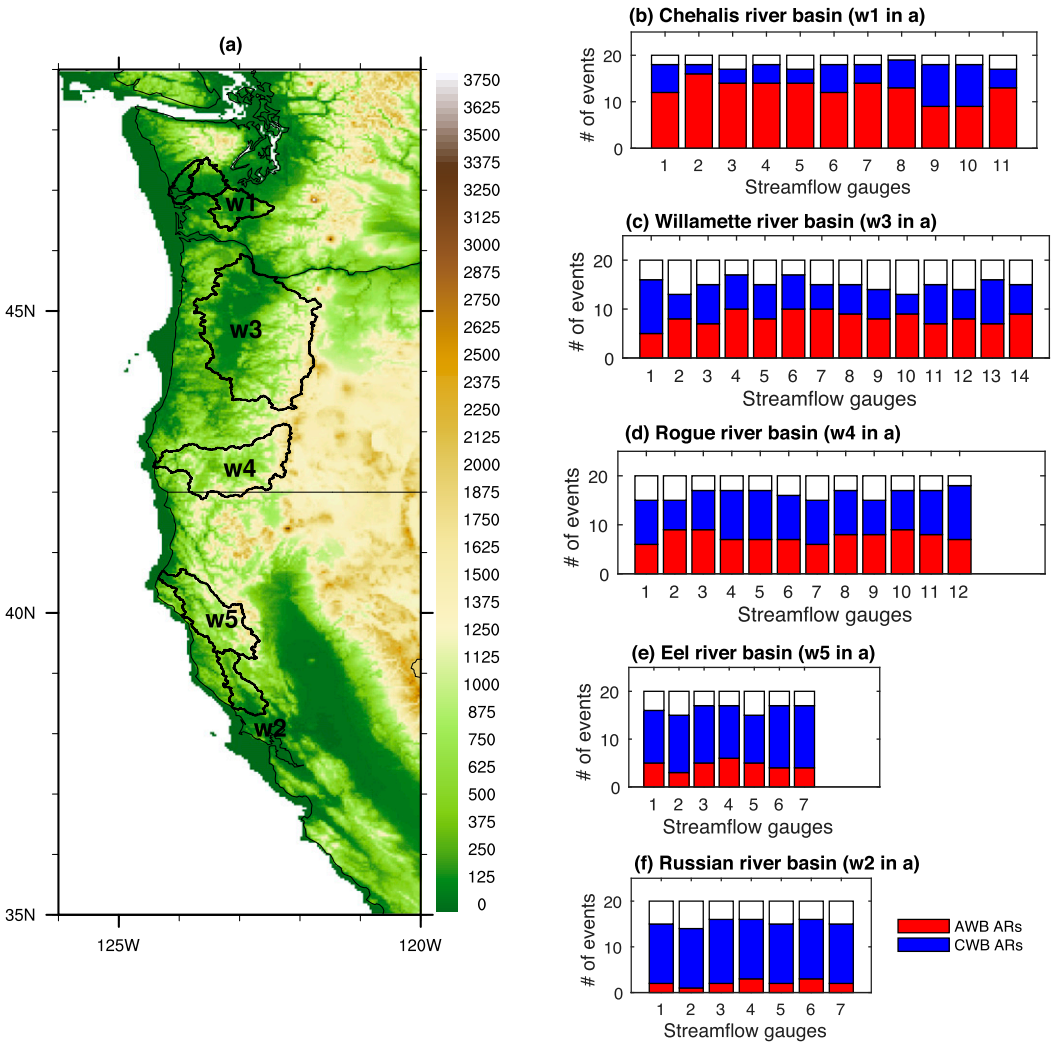

FIG. 11. (a) Shapes and locations of the five river basins along the West Coast (unit: m), and the number of top 20 streamflow events due to AWB- (red) and CWB-ARs (blue) for each USGS streamflow gauges in the (b) Chehalis, (c) Willamette, (d) Rogue, (e) Eel, and (f) Russian basins. The locations of the USGS streamflow gauges are indicated in Figs. 1b–f.

contrast, the ascent region of AWB-ARs is more spatially confined to the coast, suggesting a major orographic lifting effect. This is also consistent with the findings of Ryoo et al. (2015), where coastal ascent and anticyclonic trajectories, linked mostly to the AWB, lead to greater precipitation over the northwest coast.

As a result of the very different large-scale and synoptic features, AWB- and CWB-ARs result in different spatial patterns of precipitation and streamflow along the western coast. While precipitation is positively correlated with IVT, we find that the efficiency of converting water vapor into precipitation depends on the angle of impingement (Fig. 12). More orthogonal impingement results in higher efficiency. The impinging angles calculated from IVT show that AWB-ARs are characterized by more westerly impingement of IVT toward the coast, whereas CWB-ARs generally impinge the coast in a southwesterly direction. Consequently, the ARs will impinge on the local topography at a very different angle (assuming the angle does not change significantly from the coast).

Along the northwestern United States (Washington and Oregon), the Cascade Mountains are oriented in a north–south direction and experience higher than average precipitation during AWB-ARs. It is important to note that the optimal impinging angle for AWB-ARs to the Cascades is 40°–80° but not 90°–100°—an ideally right angle to the mountain ranges. This is because, in our period of analysis, the AR events with 90°–100° angles tend to have lower humidity and weaker IVT as the advection is from relative higher latitudes. However,

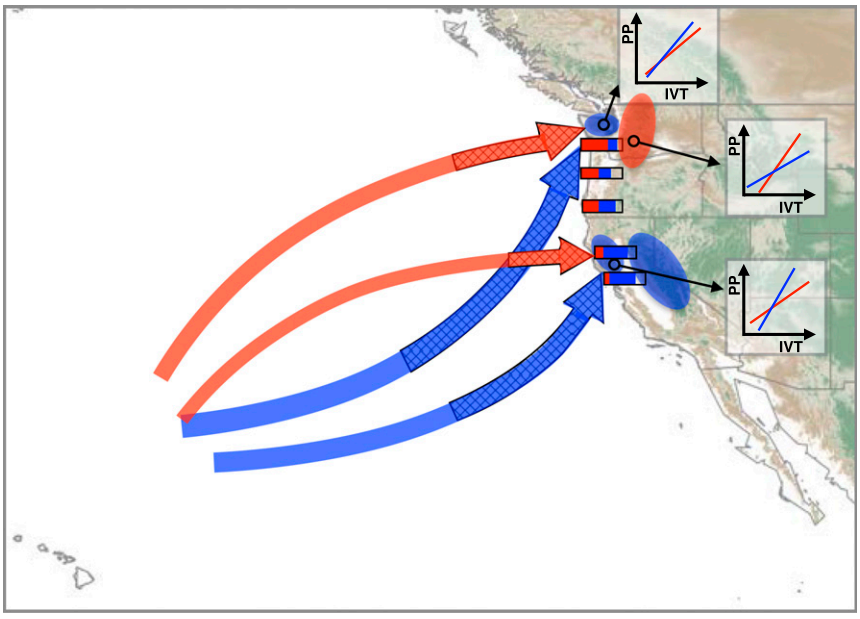

FIG. 12. Schematic showing the averaged maximum IVT axes of AWB- (thick red curves) and CWB-ARs (thick blue curves) impinging toward the northern and southern U.S. coasts (impinging angles suggested by the directions of the thick arrows). The thicknesses of the red (blue) axes suggest the magnitude of the averaged IVT magnitude associated with the AWB-ARs (CWB-ARs). The hatched part of the thick arrows suggest where ascending occur (omega $< -0.1\ \mathrm{Pa\,s^{-1}}$ at 750 mb) along the IVT axes. Red (blue) shaded ellipses suggest where positive precipitation anomaly is resulted from AWB-ARs (CWB-ARs). The compositions of the basin-averaged extreme streamflow events due to AWB-ARs (red bars) and CWB-ARs (blue bars) are shown by the horizontally aligned bars over the general basin locations. The efficiencies of AWB-ARs (CWB-ARs) in converting IVT to precipitation (or PP), obtained from the locations of the black circles, are shown by the slopes of the red (blue) lines in the x–y plots.

not all regions in the northwest show predominantly AWB-AR precipitation. A notable exception is the enhanced precipitation over the more east–west-oriented Olympic Mountains, which are predominantly affected by CWB-ARs. Accordingly, extreme streamflow events measured by the gauges in the upper Chehalis basin (draining the western Cascades) can be mostly attributed to AWB-ARs, but several gauges draining the southern Olympics within the Chehalis basin show clear signals of CWB-ARs' impact on extreme streamflow. Moving south from the Chehalis, the Willamette, Rogue, and Eel basins show progressively larger impacts of CWB-ARs on streamflow (Fig. 12). This is consistent with the latitudinal gradient of precipitation associated with AWB- and CWB-ARs.

Along the southwest U.S. coast (northern California), CWB-ARs tend to impinge normally toward the northwest–southeast-oriented mountains. In addition, over coastal California CWB-ARs are associated with stronger IVT while the strength of AWB-ARs decays rapidly at lower latitudes. These factors combined lead to greater precipitation associated with CWB-ARs along the southwest coast. As a result, in the Russian River basin of northern California, the majority of the extreme streamflow events are associated with CWB-ARs.

In this work, we focus primarily on the dynamical features associated with ARs in the upper troposphere (namely RWB) and how these features can modulate AR precipitation and associated streamflow along the West Coast. We find that AR wind direction and strength are the primary drivers of IVT intensity, extreme precipitation, and streamflow events. However, thermodynamic factors, such as temperature and moisture origin, are very important to AR strength. For instance, the multiscale AR event analyzed by Ralph et al. (2011) is marked by direct advection of water vapor from the tropics into the southern portions of the AR, as seen from satellite and dropsonde measurements. This tropical origin could contribute to the extreme nature of the event. Another extreme AR-related flooding case reported by Neiman et al. (2011), characterized by entrainment of tropical moisture, had anomalously warm conditions that resulted in more-than-usual liquid form precipitation. The thermodynamical factors are particularly important for basin-scale flooding, because these could significantly modify the rain–snow partitioning of total

precipitation. Greater than normal rain–snow partitioning can result in greatly enhanced runoff volume (White et al. 2002; Lundquist et al. 2008; Neiman et al. 2011) and could potentially lead to rain-on-snow events (Leung et al. 2004; Leung and Qian 2009). One way to examine the connections between moisture sources, thermal advection, and rain–snow partitioning—varying with climate change—is to employ finer-resolution regional models and numerical tracer tools (Sodemann and Stohl 2013) to evaluate the three-dimensional characteristics of vapor transport. This will be the topic of a future study.

In summary, depending on the associated RWB type, ARs impinge on the local topography at a different angle and have a different spatial signature of precipitation and streamflow. Our results demonstrate that large-scale upper-tropospheric dynamics can strongly modulate AR features and regional hydrologic impacts. Having established the link, questions related to how regional hydrologic impacts associated with ARs could change in a warmer climate could be investigated.

Acknowledgments. Support for this study has been provided in part by the National Aeronautics and Space Administration (NASA) Grant NNX14AD77G. Any opinions, findings, and conclusions or recommendations expressed in this publication are those of the authors and do not necessarily reflect the views of NASA. ZW acknowledges the support of National Oceanic and Atmospheric Administration (NOAA) Grants NA15NWS4680007 and NA16OAR4310080.

REFERENCES

Anders, R., K. Davidek, and D. M. Stoeckel, 2011: Water-quality data for the Russian River Basin, Mendocino and Sonoma Counties, California, 2005–2010. U.S. Geological Survey Data Series 610, 120 pp. [Available online at http://pubs.usgs.gov/ds/610/pdf/ds610.pdf.]

Barnes, E. A., and D. L. Hartmann, 2012: Detection of Rossby wave breaking and its response to shifts of the midlatitude jet with climate change. *J. Geophys. Res.*, **117**, D09117, doi:10.1029/2012JD017469.

Cayan, D. R., and J. O. Roads, 1984: Local relationships between United States West Coast precipitation and monthly mean circulation parameters. *Mon. Wea. Rev.*, **112**, 1276–1282, doi:10.1175/1520-0493(1984)112<1276:LRBUSW>2.0.CO;2.

Dettinger, M., 2011: Climate change, atmospheric rivers, and floods in California—A multimodel analysis of storm frequency and magnitude changes. *J. Amer. Water Resour. Assoc.*, **47**, 514–523, doi:10.1111/j.1752-1688.2011.00546.x.

——, F. M. Ralph, T. Das, P. J. Neiman, and D. R. Cayan, 2011: Atmospheric rivers, floods and the water resources of California. *Water*, **3**, 445–478, doi:10.3390/w3020445.

Gao, Y., J. Lu, L. R. Leung, Q. Yang, S. Hagos, and Y. Qian, 2015: Dynamical and thermodynamical modulations on future changes of landfalling atmospheric rivers over western North America. *Geophys. Res. Lett.*, **42**, 7179–7186, doi:10.1002/2015GL065435.

Guan, B., and D. E. Waliser, 2015: Detection of atmospheric rivers: Evaluation and application of an algorithm for global studies. *J. Geophys. Res. Atmos.*, **120**, 12 514–12 535, doi:10.1002/2015JD024257.

——, N. P. Molotch, D. E. Waliser, E. J. Fetzer, and P. J. Neiman, 2010: Extreme snowfall events linked to atmospheric rivers and surface air temperature via satellite measurements. *Geophys. Res. Lett.*, **37**, L20401, doi:10.1029/2010GL044696.

Hagos, S., L. R. Leung, Q. Yang, C. Zhao, and J. Lu, 2015: Resolution and dynamical core dependence of atmospheric river frequency in global model simulations. *J. Climate*, **28**, 2764–2776, doi:10.1175/JCLI-D-14-00567.1.

Hayes, J. L., 2008: Service assessment—Pacific Northwest storms of December 1-3, 2007. NOAA, 39 pp. [Available online at http://www.weather.gov/media/publications/assessments/pac_nw08.pdf.]

Hoskins, B. J., A. J. Simmons, and D. G. Andrews, 1977: Energy dispersion in a barotropic atmosphere. *Quart. J. Roy. Meteor. Soc.*, **103**, 553–567, doi:10.1002/qj.49710343802.

Lavers, D. A., G. Villarini, R. P. Allan, E. F. Wood, and A. J. Wade, 2012: The detection of atmospheric rivers in atmospheric reanalyses and their links to British winter floods and the large-scale climatic circulation. *J. Geophys. Res.*, **117**, D20106, doi:10.1029/2012JD018027.

——, R. P. Allan, G. Villarini, B. Lloyd-Hughes, D. J. Brayshaw, and A. J. Wade, 2013: Future changes in atmospheric rivers and their implications for winter flooding in Britain. *Environ. Res. Lett.*, **8**, 034010, doi:10.1088/1748-9326/8/3/034010.

Leung, L. R., and Y. Qian, 2009: Atmospheric rivers induced heavy precipitation and flooding in the western U.S. simulated by the WRF regional climate model. *Geophys. Res. Lett.*, **36**, L03820, doi:10.1029/2008GL036445.

——, ——, X. Bian, W. M. Washington, J. Han, and J. O. Roads, 2004: Mid-century ensemble regional climate change scenarios for the western United States. *Climatic Change*, **62**, 75–113, doi:10.1023/B:CLIM.0000013692.50640.55.

L'Heureux, M. L., and D. Thompson, 2006: Observed relationships between the El Niño–Southern Oscillation and the extratropical zonal-mean circulation. *J. Climate*, **19**, 276–287, doi:10.1175/JCLI3617.1.

Liu, C., and E. A. Barnes, 2015: Extreme moisture transport into the Arctic linked to Rossby wave breaking. *J. Geophys. Res. Atmos.*, **120**, 3774–3788, doi:10.1002/2014JD022796.

Livneh, B., E. A. Rosenberg, C. Lin, B. Nijssen, V. Mishra, K. Andreadis, E. Maurer, and D. Lettenmaier, 2013: A long-term hydrologically based dataset of land surface fluxes and states for the conterminous United States: Update and extensions. *J. Climate*, **26**, 9384–9392, doi:10.1175/JCLI-D-12-00508.1.

Lundquist, J. D., P. J. Neiman, B. Martner, A. B. White, D. J. Gottas, and F. M. Ralph, 2008: Rain versus snow in the Sierra Nevada, California: Comparing Doppler profiling radar and surface observations of melting level. *J. Hydrometeor.*, **9**, 194–211, doi:10.1175/2007JHM853.1.

Mass, C., A. Skalenakis, and M. Warner, 2011: Extreme precipitation over the West Coast of North America: Is there a trend? *J. Hydrometeor.*, **12**, 310–318, doi:10.1175/2010JHM1341.1.

McIntyre, M. E., and T. N. Palmer, 1985: A note on the general concept of wave breaking for Rossby and gravity waves. *Pure Appl. Geophys.*, **123**, 964–975, doi:10.1007/BF00876984.

Messori, G., and R. Caballero, 2015: On double Rossby wave breaking in the North Atlantic. *J. Geophys. Res. Atmos.*, **120**, 11 129–11 150, doi:10.1002/2015JD023854.

Moore, B. J., P. J. Neiman, F. M. Ralph, and F. Barthold, 2012: Physical processes associated with heavy flooding rainfall in Nashville, Tennessee, and vicinity during 1–2 May 2010: The role of an atmospheric river and mesoscale convective systems. *Mon. Wea. Rev.*, **140**, 358–378, doi:10.1175/MWR-D-11-00126.1.

Mundhenk, B. D., E. A. Barnes, and E. D. Maloney, 2016a: All-season climatology and variability of atmospheric river frequencies over the North Pacific. *J. Climate*, **29**, 4885–4903, doi:10.1175/JCLI-D-15-0655.1.

——, ——, ——, and K. M. Nardi, 2016b: Modulation of atmospheric rivers near Alaska and the U.S. West Coast by northeast Pacific height anomalies. *J. Geophys. Res. Atmos.*, **121**, 12751–12765, doi:10.1002/2016JD025350.

Nakamura, M., and R. A. Plumb, 1994: The effects of flow asymmetry on the direction of Rossby wave breaking. *J. Atmos. Sci.*, **51**, 2031–2045, doi:10.1175/1520-0469(1994)051<2031:TEOFAO>2.0.CO;2.

Neiman, P. J., F. M. Ralph, G. A. Wick, Y.-H. Kuo, T.-K. Wee, Z. Ma, G. H. Taylor, and M. D. Dettinger, 2008a: Diagnosis of an intense atmospheric river impacting the Pacific Northwest: Storm summary and offshore vertical structure observed with COSMIC satellite retrievals. *Mon. Wea. Rev.*, **136**, 4398–4420, doi:10.1175/2008MWR2550.1.

——, ——, ——, J. D. Lundquist, and M. D. Dettinger, 2008b: Meteorological characteristics and overland precipitation impacts of atmospheric rivers affecting the West Coast of North America based on eight years of SSM/I satellite observations. *J. Hydrometeor.*, **9**, 22–47, doi:10.1175/2007JHM855.1.

——, L. J. Schick, and F. M. Ralph, 2011: Flooding in western Washington: The connection to atmospheric rivers. *J. Hydrometeor.*, **12**, 1337–1358, doi:10.1175/2011JHM1358.1.

Orlanski, I., 2005: A new look at the Pacific storm track variability: Sensitivity to tropical SSTs and to upstream seeding. *J. Atmos. Sci.*, **62**, 1367–1390, doi:10.1175/JAS3428.1.

Payne, A. E., and G. Magnusdottir, 2014: Dynamics of landfalling atmospheric rivers over the North Pacific in 30 years of MERRA reanalysis. *J. Climate*, **27**, 7133–7150, doi:10.1175/JCLI-D-14-00034.1.

Peters, D., and D. W. Waugh, 1996: Influence of barotropic shear on the poleward advection of upper-tropospheric air. *J. Atmos. Sci.*, **53**, 3013–3031, doi:10.1175/1520-0469(1996)053<3013:IOBSOT>2.0.CO;2.

Ralph, F. M., and M. D. Dettinger, 2011: Storms, floods, and the science of atmospheric rivers. *Eos, Trans. Amer. Geophys. Union*, **92**, 265–266, doi:10.1029/2011EO320001.

——, and ——, 2012: Historical and national perspectives on extreme West Coast precipitation associated with atmospheric rivers during December 2010. *Bull. Amer. Meteor. Soc.*, **93**, 783–790, doi:10.1175/BAMS-D-11-00188.1.

——, P. J. Neiman, D. E. Kingsmill, P. O. G. Persson, E. T. Strem, E. D. Andrews, and R. C. Antweiler, 2003: The impact of a prominent rain shadow on flooding in California's Santa Cruz Mountains: A CALJET case study and sensitivity to the ENSO cycle. *J. Hydrometeor.*, **4**, 1243–1264, doi:10.1175/1525-7541(2003)004<1243:TIOAPR>2.0.CO;2.

——, ——, and G. A. Wick, 2004: Satellite and CALJET aircraft observations of atmospheric rivers over the eastern North Pacific Ocean during the winter of 1997/98. *Mon. Wea. Rev.*, **132**, 1721–1745, doi:10.1175/1520-0493(2004)132<1721:SACAOO>2.0.CO;2.

——, ——, ——, S. I. Gutman, M. D. Dettinger, D. R. Cayan, and A. B. White, 2006: Flooding on California's Russian River: Role of atmospheric rivers. *Geophys. Res. Lett.*, **33**, L13801, doi:10.1029/2006GL026689.

——, ——, G. N. Kiladis, K. Weickmann, and D. W. Reynolds, 2011: A multiscale observational case study of a Pacific atmospheric river exhibiting tropical–extratropical connections and a mesoscale frontal wave. *Mon. Wea. Rev.*, **139**, 1169–1189, doi:10.1175/2010MWR3596.1.

——, T. Coleman, P. J. Neiman, R. J. Zamora, and M. D. Dettinger, 2013: Observed impacts of duration and seasonality of atmospheric-river landfalls on soil moisture and runoff in coastal Northern California. *J. Hydrometeor.*, **14**, 443–459, doi:10.1175/JHM-D-12-076.1.

Rienecker, M. M., and Coauthors, 2011: MERRA: NASA's Modern-Era Retrospective Analysis for Research and Applications. *J. Climate*, **24**, 3624–3648, doi:10.1175/JCLI-D-11-00015.1.

Ruckelshaus Center, 2012: Chehalis basin flood hazard mitigation alternatives report. Washington State University, 532 pp. [Available online at http://ruckelshauscenter.wsu.edu/wp-content/uploads/2013/06/chehalis-report-12-19-12.pdf.]

Rutz, J. J., W. J. Steenburgh, and F. M. Ralph, 2014: Climatological characteristics of atmospheric rivers and their inland penetration over the western United States. *Mon. Wea. Rev.*, **142**, 905–921, doi:10.1175/MWR-D-13-00168.1.

Ryoo, J.-M., Y. Kaspi, D. W. Waugh, G. N. Kiladis, D. E. Waliser, E. J. Fetzer, and J. Kim, 2013: Impact of Rossby wave breaking on U.S. West Coast winter precipitation during ENSO events. *J. Climate*, **26**, 6360–6382, doi:10.1175/JCLI-D-12-00297.1.

——, D. E. Waliser, D. W. Waugh, S. Wong, E. J. Fetzer, and I. Fung, 2015: Classification of atmospheric river events on the U.S. West Coast using a trajectory model. *J. Geophys. Res. Atmos.*, **120**, 3007–3028, doi:10.1002/2014JD022023.

Salathé, E. P., Jr., 2006: Influences of a shift in North Pacific storm tracks on western North American precipitation under global warming. *Geophys. Res. Lett.*, **33**, L19820–L19824, doi:10.1029/2006GL026882.

Seager, R., N. Harnik, Y. Kushnir, W. Robinson, and J. Miller, 2003: Mechanisms of hemispherically symmetric climate variability. *J. Climate*, **16**, 2960–2978, doi:10.1175/1520-0442(2003)016<2960:MOHSCV>2.0.CO;2.

Sodemann, H., and A. Stohl, 2013: Moisture origin and meridional transport in atmospheric rivers and their association with multiple cyclones. *Mon. Wea. Rev.*, **141**, 2850–2868, doi:10.1175/MWR-D-12-00256.1.

Strong, C., and G. Magnusdottir, 2008: How Rossby wave breaking over the Pacific forces the North Atlantic Oscillation. *Geophys. Res. Lett.*, **35**, L10706, doi:10.1029/2008GL033578.

Thorncroft, C. D., B. J. Hoskins, and M. E. McIntyre, 1993: Two paradigms of baroclinic-wave life-cycle behaviour. *Quart. J. Roy. Meteor. Soc.*, **119**, 17–55, doi:10.1002/qj.49711950903.

Wang, Z., and C.-P. Chang, 2012: A numerical study of the interaction between the large-scale monsoon circulation and orographic precipitation over South and Southeast Asia. *J. Climate*, **25**, 2440–2455, doi:10.1175/JCLI-D-11-00136.1.

Warner, M. D., C. F. Mass, and E. P. Salathé Jr., 2012: Wintertime extreme precipitation events along the Pacific Northwest

coast: Climatology and synoptic evolution. *Mon. Wea. Rev.*, **140**, 2021–2043, doi:10.1175/MWR-D-11-00197.1.

White, A. B., D. J. Gottas, E. T. Strem, F. Ralph, and P. Neiman, 2002: An automated brightband height detection algorithm for use with Doppler radar spectral moments. *J. Atmos. Oceanic Technol.*, **19**, 687–697, doi:10.1175/1520-0426(2002)019<0687:AABHDA>2.0.CO;2.

Wick, G. A., P. J. Neiman, and F. M. Ralph, 2013: Description and validation of an automated objective technique for identification and characterization of the integrated water vapor signature of atmospheric rivers. *IEEE Trans. Geosci. Remote Sens.*, **51**, 2166–2176, doi:10.1109/TGRS.2012.2211024.

Zhu, Y., and R. E. Newell, 1994: Atmospheric rivers and bombs. *Geophys. Res. Lett.*, **21**, 1999–2002, doi:10.1029/94GL01710.

——, and ——, 1998: A proposed algorithm for moisture fluxes from atmospheric rivers. *Mon. Wea. Rev.*, **126**, 725–735, doi:10.1175/1520-0493(1998)126<0725:APAFMF>2.0.CO;2.